Hindawi
International Journal of Energy Research
Volume 2023, Article ID 8011817, 12 pages
https://doi.org/10.1155/2023/8011817

Research Article

Untethered Nanotextured Thermopneumatic Soft Actuators Operable with Different Stimuli: Thermal Blowing, Infrared Light, and Electromagnetic Field

Yong Il Kim,[1] Si Wung Kim,[2] Seongpil An,[3] Alexander L. Yarin,[1,2] and Sam S. Yoon[2]

[1]*Department of Mechanical & Industrial Engineering, University of Illinois at Chicago, 842 W. Taylor St., Chicago 60607, USA*
[2]*School of Mechanical Engineering, Korea University, Seoul 02841, Republic of Korea*
[3]*SKKU Advanced Institute of Nanotechnology (SAINT), Department of Nano Science and Technology, Department of Nano Engineering, and Department of Semiconductor Convergence Engineering, Sungkyunkwan University, Suwon 16419, Republic of Korea*

Correspondence should be addressed to Seongpil An; esan@skku.edu, Alexander L. Yarin; ayarin@uic.edu, and Sam S. Yoon; skyoon@korea.ac.kr

Received 17 February 2023; Revised 13 May 2023; Accepted 24 May 2023; Published 22 June 2023

Academic Editor: Kathiravan Srinivasan

In this study, untethered nanotextured thermopneumatic soft actuators (UTPSAs) were developed using a soft elastomer body encapsulating a volatile fluid (Novec 7000), which underwent a phase change (evaporation) when stimuli that convert energy into heat were applied using wireless transmission. Herein, we analyzed three types of stimuli: (i) thermal blowing, (ii) irradiation with infrared light, and (iii) electromagnetic energy transmission. In the third case, an electromagnetic field induced an electric current in a wire coil embedded in an elastomeric body, thus providing Joule heating to induce fluid evaporation. The bending curvature and force generated during bending were examined under various operational conditions, which enable one to select the optimal operating mechanism of UTPSAs for a specific environment. Specifically, diverse operating capabilities of UTPSAs are expected to be useful in dynamic environments, e.g., rescue situations. In addition, as a potential application, a crawler-configured UTPSA was fabricated, and its operation was demonstrated.

1. Introduction

In the research community, soft robots have received considerable attention as a novel type of biocompatible robots made of soft, flexible, and biocompatible materials [1, 2]. Unlike conventional rigid robots, which possess six degrees of freedom, soft robots can possess additional degrees of freedom [3]. Therefore, they can imitate various biological systems with multiple degrees of freedom [4]. In addition, soft robots capable of changing their shapes according to environments can help effectively handle fragile objects [5]. Moreover, they are durable, can withstand strong impact without losing their basic motion, and do not require complicated computer calculations [6].

Studies of soft robots focus on two topics: (i) soft materials constituting the robot body and (ii) working mechanisms enabling deformation/movement [7]. The soft materials are electroactive polymers [8, 9], thermoresponsive elastomers [10], pH- or solvent-responsive gels [11–13], paper [14], carbonaceous materials [15], and fluids [16, 17]. The actuation mechanisms of these robots are performed using soft actuators that can be triggered by external stimuli, e.g., electric or magnetic field, temperature variation, chemical reactions, and pressure changes [18–21]. Although several studies focused on soft actuators, the actuators need to be further enhanced for commercial feasibility because they require high energy consumption [8], external auxiliary equipment [22, 23], and specific environments to perform effectively [16, 24].

An et al. developed a novel thermopneumatic soft actuator to address the aforementioned issues [7, 25]. The actuator can perform continuous movements based on the

volume expansion/contraction that occurs during the phase change of the fluid inside the actuator body (e.g., a volatile fluid) triggered by thermal energy. However, it had limitations: slow movements and operation for a few cycles. Moreover, as an external heater chamber was required, the actuator was inefficient in terms of space utilization and energy consumption.

Thus, two in-depth studies were conducted to address the limitations of the thermopneumatic soft actuator based on materials and structures [26, 27]. First, the body and internal phase change materials were modified. Faster and more durable performance was achieved by adding nanomaterials to the body material considering high thermal conductivity. Moreover, the replacement of the internal fluid capable of phase change at low temperatures improved the speed of the soft robot. Second, a heating wire was inserted into the thermopneumatic soft actuator to develop a heat source in the actuator body, thereby eliminating the need for an external heater and maximizing energy efficiency.

This study is aimed at improving the performance of thermopneumatic soft actuators based on a different perspective, which was not considered in the aforementioned studies. We developed an untethered nanotextured thermopneumatic soft actuator (UTPSA) that can be activated by various heat transfer methods. Herein, convection and radiation, which are generated by thermal blower and infrared light, respectively, were considered for remote heat transfer. In addition, a system that generates heat inside a UTPSA based on electromagnetic induction was implemented. Further, we demonstrated that the UTPSA can be operated using three types of wireless stimuli—thermal blowing, infrared light, or an electromagnetic field. Then, the performance of the UTPSA was comprehensively examined by placing obstacles between the UTPSA and stimulus source. Finally, a crawler-configured UTPSA was fabricated, and its performance was evaluated. The source used in the present actuator was smaller and easier to control remotely than those used in other studies [28–30]. The developed UTPSA that can select an optimal operating mechanism for a specific situation can be effectively used in dynamic environments, e.g., rescue situations.

2. Results and Discussion

2.1. Untethered Thermopneumatic Soft Actuator (UTPSA). Figure 1(a) depicts the proposed UTPSA comprising six layers: (I) Ecoflex body, (II) liquid storage, (III) blocking, (IV) heater wire, (V) Ecoflex body, and (VI) passive. The UTPSA fabrication process is detailed in Section S1 of the Supplementary Information section. The Ecoflex bodies (the first and fifth layers) constitute the skeleton of the UTPSA, which includes the encapsulated liquid/vapor. The liquid storage layer comprises polyacrylonitrile nanofibers (PAN NFs), which possess numerous interfiber pores. Therefore, it can absorb a large amount of fluid (Novec 7000) [7]. Novec 7000 is a liquid with a low boiling point (approximately 34°C). Accordingly, a large volume change inside the UTPSA can be achieved based on the phase change of Novec 7000 under relatively minor heating. Novec 7000 is stored in the liquid storage layer and used to operate the UTPSA. A blocking layer is placed on top of the NF mat (the third step in Figure S1a) to prevent the PAN mat from moisture caused by the Ecoflex layer formed at the fifth step (Figure S1a). The heater wire layer is used to apply Joule heating to the Novec 7000 via external electromagnetically generated electric current. The stiff passive layer enables the UTPSA to deform (or expand) anisotropically (Figure 1(b)) [25, 26], whereas a UTPSA without such a passive layer deforms (or expands) isotropically, similar to a balloon (Movie S1). Figure 1(b) shows the actuating mechanism of the UTPSA. As the temperature (T) of the fluid (i.e., Novec 7000 inside the UTPSA) exceeds the liquid-vapor phase change temperature (T_B), a phase change occurs from the liquid to the vapor state, thereby significantly expanding the UTPSA volume. The expansion of the UTPSA leads to the unidirectional bending of the UTPSA owing to the presence of the passive layer.

To evaluate the actuating performance of the UTPSA with regard to its output bending force, a force gauge was placed perpendicular to the bending direction of the UTPSA (Figure 1(c)). In addition, the displacements between the three locations (x_n and y_n, $n = 1, 2, 3$) on the body of the UTPSA were measured to determine the degree of bending (Figure S2). For example, variations in the displacements were converted into curvature values, and the bending rate was obtained using the curvature values over time. These methods are detailed in Section S2 of the Supplementary Information.

Figure 1(d) shows the operation of the UTPSA based on three different types of wireless stimuli: thermal blowing, infrared light, and electromagnetic field. Thermal blowing was performed using a heating gun, infrared light was applied using a high-intensity lamp, and an electromagnetic field was generated using a wireless charging module (Section S1.4). All the stimuli can propagate in the air; however, not through the obstacles (left-hand side images of Figure 1(d)). For instance, thermal blowing cannot penetrate transparent or opaque obstacles (a glass with a thickness of 3.75 mm and an alumina substrate with a thickness of 0.635 mm were used as transparent and opaque obstacles, respectively). Infrared light could not supply sufficient energy to the UTPSA when an alumina obstacle was used. The electromagnetic field can penetrate the obstacles that possess low conductivity (e.g., glass, alumina, wood, and concrete) [31]. Thus, it can be used to supply energy remotely to the UTPSA under various obstacles. When the UTPSA was sufficiently exposed to any of these stimuli, the encased fluid was heated (by thermal blowing, infrared light, or electromagnetic induction), and a phase change was induced in the fluid. This caused volume expansion, which resulted in an anisotropic expansion of the UTPSA, facilitating bending motion (right-hand side images of Figure 1(d)).

An activated (or bent) UTPSA can return to its initial inactive state via vapor condensation caused by natural or artificial cooling. Figure 1(e) presents the curvature change of the UTPSA as its internal pressure varies. As the internal pressure increased from 0 to 1.04 bar, the corresponding curvature of the UTPSA increased slightly from 0 to 5 m^{-1}.

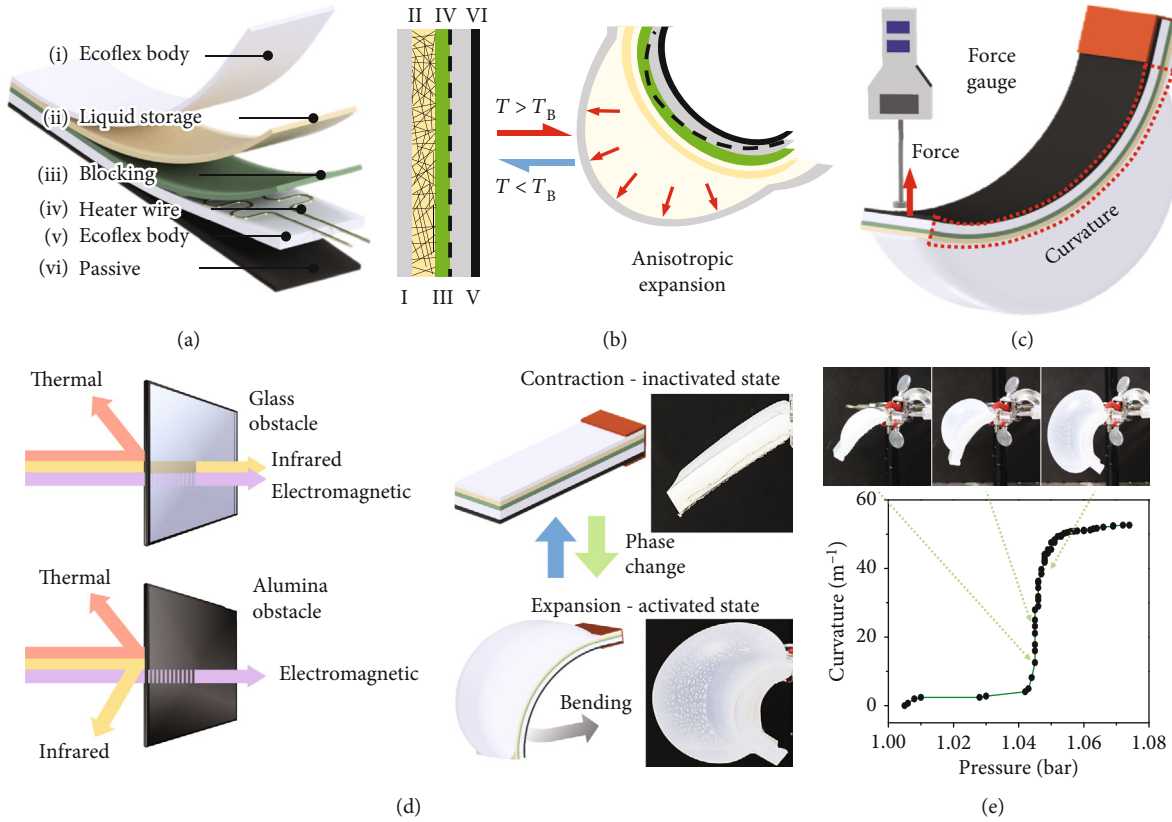

Figure 1: (a) Overall structure and (b) the working principle of the UTPSA. (c) Measurement of the output force and curvature of the UTPSA and (d) UTPSA operation triggered by three different types of wireless stimuli. (e) Change in the curvature of the UTPSA with the internal pressure.

However, a significant increase in the curvature was observed (from 5 to 46 m^{-1}) beyond 1.04 bar (after which the pressure remained almost constant), resulting in faster bending motion than that observed in the initial curvature range of 0–5 m^{-1}.

Figure 2(a) presents a calorimetric comparison of the different types of fluid, considering the specific heat required to achieve the boiling temperature Q_h and latent heat required for evaporation Q_b. Ethanol, which is widely used as a phase change material in soft actuators [32, 33], was analyzed to confirm the benefits of Novec 7000. Low thermal energy is required to evaporate Novec 7000, and its boiling point (34°C) is also low. This enabled the most efficient volume expansion of the UTPSA (practically at room temperature), under the three wireless stimuli. Furthermore, Novec 7000 is electrically stable, nontoxic to human skin [34, 35], and promising for body-attachable or wearable soft robotics [36]. In addition, as Novec 7000 possesses higher vapor pressure than ethanol (Figure 2(b)), higher pressure can be generated (and thus higher output force and curvature) with less thermal energy.

2.2. Operation of the UTPSA under Wireless Stimuli. Figure 3(a) shows the experimental setup for the wireless operation of the UTPSA via thermal blowing using a heat gun. The experiments were performed at 26°C (room temperature) in open air. The thermal gun was located at 20, 40, 60, and 80 cm from the UTPSA, and the changes in the UTPSA were observed (Section S1.6). Under thermal blowing, the temperature around the UTPSA increased for approximately 40 s, after which it became constant at 119, 87, 66, and 42°C for distances of 20, 40, 60, and 80 cm, respectively (Figure 3(b)). In open environments, the farther the distance between the heat gun and UTPSA, the less effective the heat gun because of an unrelated external wind could become dominant. This might result in temperature fluctuations in the 80 cm case, and it should be carefully considered while designing UTPSA applications. After an obstacle was placed between the heat gun and UTPSA, there was no change in the temperature of the UTPSA (Figure S3).

The experimental setup for UTPSA activation using infrared light is shown in Figure 3(c). A lamp was installed at a distance of 5–50 cm (in increments of 5 cm) from the UTPSA. Figure 3(d) illustrates the variation in irradiance intensity with an increase in the distance. The maximum irradiance measured by the solar meter was 4000 $W{\cdot}m^{-2}$ at 5 cm. The irradiance intensity gradually decreased from 4000 to 3888, 2571, 2229, 1637, 1152, 909, 623, 495, and 322 $W{\cdot}m^{-2}$ as the distance increased. When the glass was positioned between the lamp and UTPSA, the overall irradiance intensity decreased by approximately 40% compared to that observed without the obstacle. This was attributed to light absorption or reflection by the glass

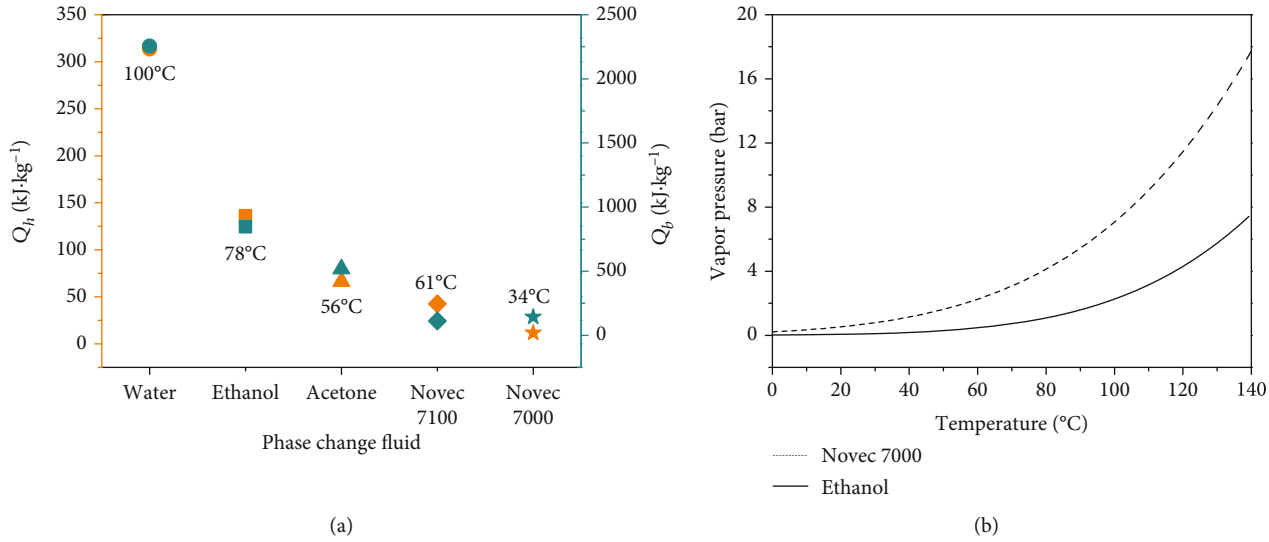

FIGURE 2: (a) Specific heat required to increase the temperature of each fluid from 25°C to its boiling point (orange). The panel also lists the boiling point of each fluid. Latent heat generated by fluid evaporation (cyan). (b) Change in the vapor pressure of two volatile fluids with the temperature.

[37]. When an alumina substrate was used as an obstacle, it reduced the irradiance by 82%–97% compared to that for the case without the obstacle.

Figure S4a presents the temperature around the light lamp when the glass obstacle is present. As the glass possessed low reflectance (<10%) with respect to infrared/visible light, the temperature increase around the lamp induced by the reflected light was not high [38]. By contrast, a higher temperature rise was observed when alumina was used as an obstacle because of its high reflectance (>80% with respect to infrared/visible light [39]) (Figure S4b). Figure S5 illustrates the transmittance profiles of each type of obstacle, which are consistent with the results presented in Figure 3(d) and Figure S4. Consequently, only the light through the glass obstacle is absorbed by the UTPSA, increasing the temperature of the internal fluid. It induces the phase change and volume expansion of the fluid and allows the UTPSA to operate.

Figure 3(e) depicts the setup for the short-distance remote operation of the UTPSA using a wireless charging module consisting of two coils: (i) a transmission coil connected to a power supply to generate an electromagnetic field and (ii) a receiving coil that converts the electromagnetic field into electricity and supplies an electric current directly to the UTPSA. In this case, the wireless power transmission was generated via magnetic induction using a commercial, reliable, economic wireless module. The distances between the two coils were set to 0, 0.6, 1.2, and 1.8 cm. When the receiving coil transmitted electromagnetic energy to the UTPSA via electromagnetic induction, Joule heating occurred owing to the heating wire embedded in the UTPSA. Accordingly, the temperature of the internal fluid in the UTPSA increased, and its volume began to expand owing to evaporation. Finally, the UTPSA began to bend as in the other two cases. Figure 3(f) presents the energy conversion efficiency as a function of the distance between the two coils (transmitter and receiver). The input voltage V_{input} was fixed at 12 V using an Arduino module, whereas the input supplied current I_{input} and input power P_{input} changed according to the coil distance. The mutual inductance between the two coils affects not only an input current but also an output current. As the distance increased, both P_{input} and the electromagnetically induced output power P_{output} (measured at the receiver coil) gradually decreased.

An almost constant energy conversion efficiency ($= P_{output}/P_{input} \times 100\%$) was observed up to a distance of 1.5 cm (Figure 3(f)). Once the distance increased to 1.8 cm, negligible electromagnetic energy could be transmitted, resulting in a significantly decreased efficiency (by approximately 20%). The correlation between the efficiency and distance is consistent with the study of Lho [40]. Although the working distance based on the module used in this study was limited to 1.8 cm, it can be further increased by improving the operating conditions and coil design [41, 42]. Solid obstacles (i.e., glass and alumina) negligibly affect the electromagnetic field in contrast to thermal blowing and infrared light. The infrared images of the heating wire connected to the receiver coil are shown in Figure 3(g) (cf. Figure S1). As the distance between the coils increased to 1.2 cm, the heating wire temperature was almost constant at >34°C but decreased to approximately 30°C at 1.8 cm.

2.3. Performance of the UTPSA during Bending Actuation. Figure 4(a) illustrates the change in the curvature of the UTPSA with respect to the distance between the thermal blowing source and UTPSA. A cycle of bending and straightening motions was observed for each distance. The stretching (or unfolding) motion was performed by discharging the internal vapor using a suction motor (Figure S1) to shorten the process of converting the vapor to liquid. However, this study is aimed at remotely inducing a

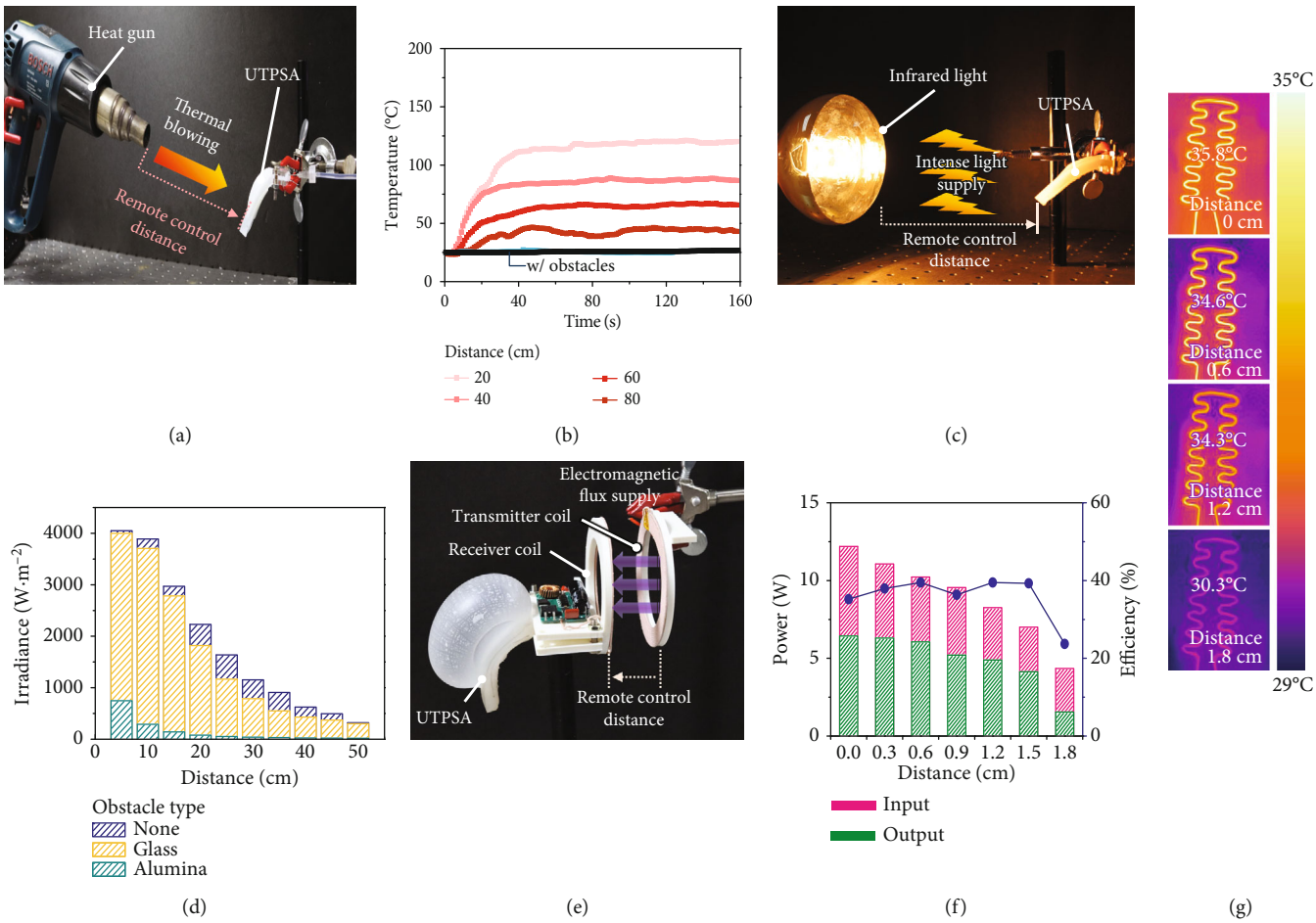

FIGURE 3: Experimental setups for the analysis of UTPSA operations considering (a) thermal blowing, (c) infrared light, and (e) electromagnetic field. Profiles of (b) temperature increase due to thermal blowing, (d) irradiance power associated with infrared light according to the distance from the UTPSA, and (f) induced power caused by the electromagnetic field according to the distance between coils, with and without obstacles. (g) The infrared images of the heating wire operated based on the electromagnetically induced electric power of the wireless module.

bending motion using various types of stimuli. The times required to complete a cycle were 88, 145, 305, and 455 s when the nozzle distances were 20, 40, 60, and 80 cm, respectively, demonstrating that the high heat flux enabled the UTPSA to respond faster when the distance was shorter. The maximum curvature value of all the cases was approximately 48 m^{-1}, beyond which is difficult to achieve using a UTPSA (as evident from Figure 1(e)). Figure 4(b) shows the corresponding force derived from the bending UTPSA using the setup shown in Figure 1(c). Although the maximum bending curvature was similar regardless of the distance, the force derived from the UTPSA decreased as the distance increased. The maximum force decreased from 900 to 840, 600, and 520 mN as the distance increased from 20 to 40, 60, and 80 cm, respectively. At some point, the side of the passive layer remained stationary, while the opposite side swelled. In other words, although the internal pressure of the UTPSA increased, the curvature and force did not change.

Similarly, the change in the curvature while using infrared light was examined for various distances between the lamp and UTPSA (Figure 4(c)). The times required for a cycle at 5, 10, 15, and 20 cm were 124, 179, 266, and 336 s, respectively, which seems faster compared to the thermal case but slower considering the distance value, and the maximum curvature values were 49, 46, 45, and 44 m^{-1}, respectively, which is similar to the previous case (approximately 48 m^{-1}). As shown in Figure 4(d), the corresponding maximum force decreased from 800 to 600, 480, and 280 mN as the distance increased. The decreasing rate of force according to the distance was much larger compared to the thermal case.

Figure 4(e) depicts the change in curvature with time for the UTPSA operating in a bending-straightening motion using an electromagnetic field. The distances between coils were 0, 0.6, 1.2, and 1.8 cm, which are much shorter compared to other cases; in this case, the times required for a single cycle were 313, 328, 351, and 371 s, respectively, i.e., the time was nearly constant regardless of the increase in the distance between the coils. The maximum curvature values were similar: 46, 45, 42, and 40 m^{-1} at 0, 0.6, 1.2, and 1.8 cm, respectively. The change in the bending force of the UTPSA as a function of time is illustrated in Figure 4(f). The maximum force associated with bending decreased from 610 to 565, 270, and 196 mN at coil distances

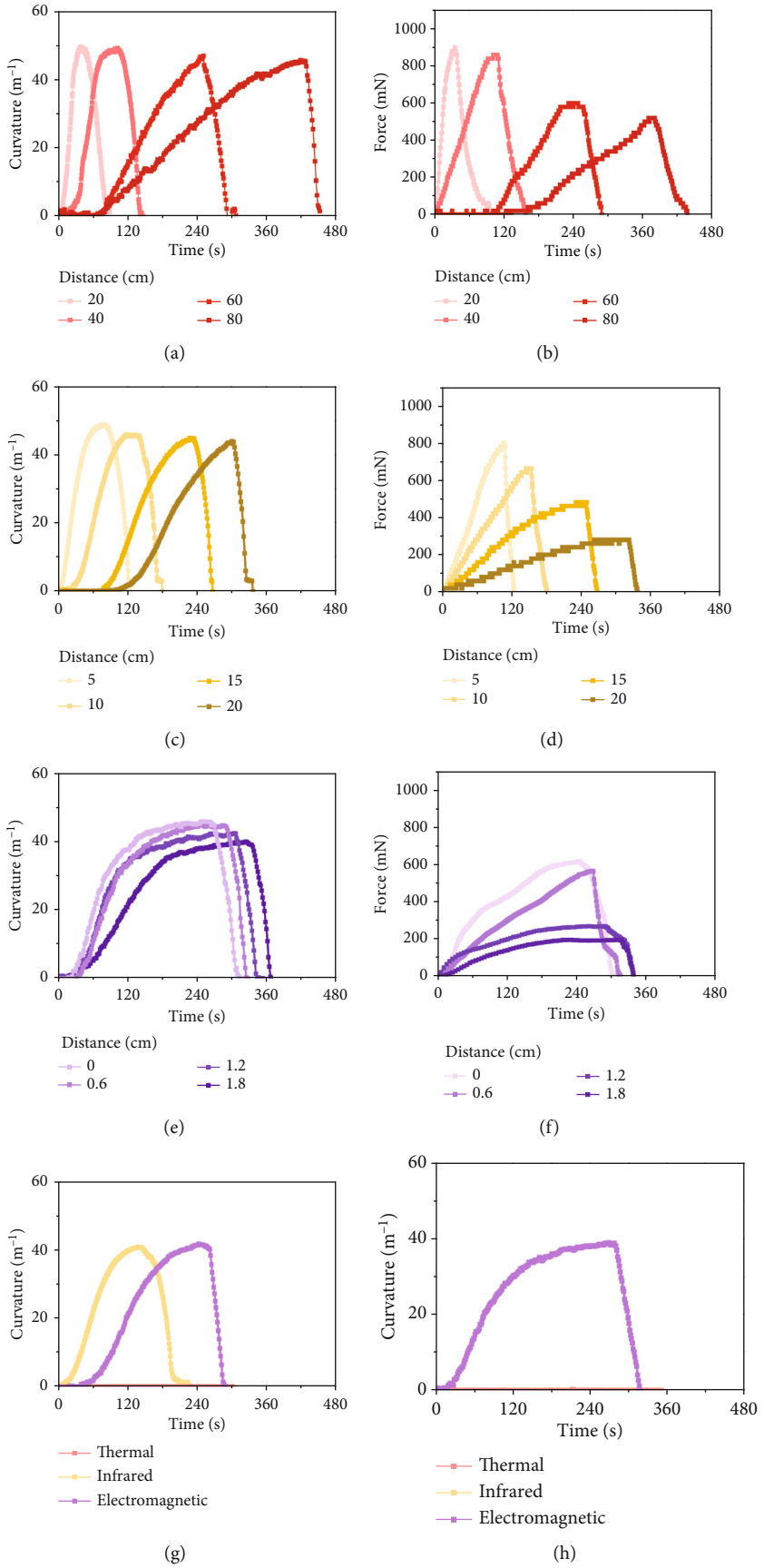

Figure 4: Continued.

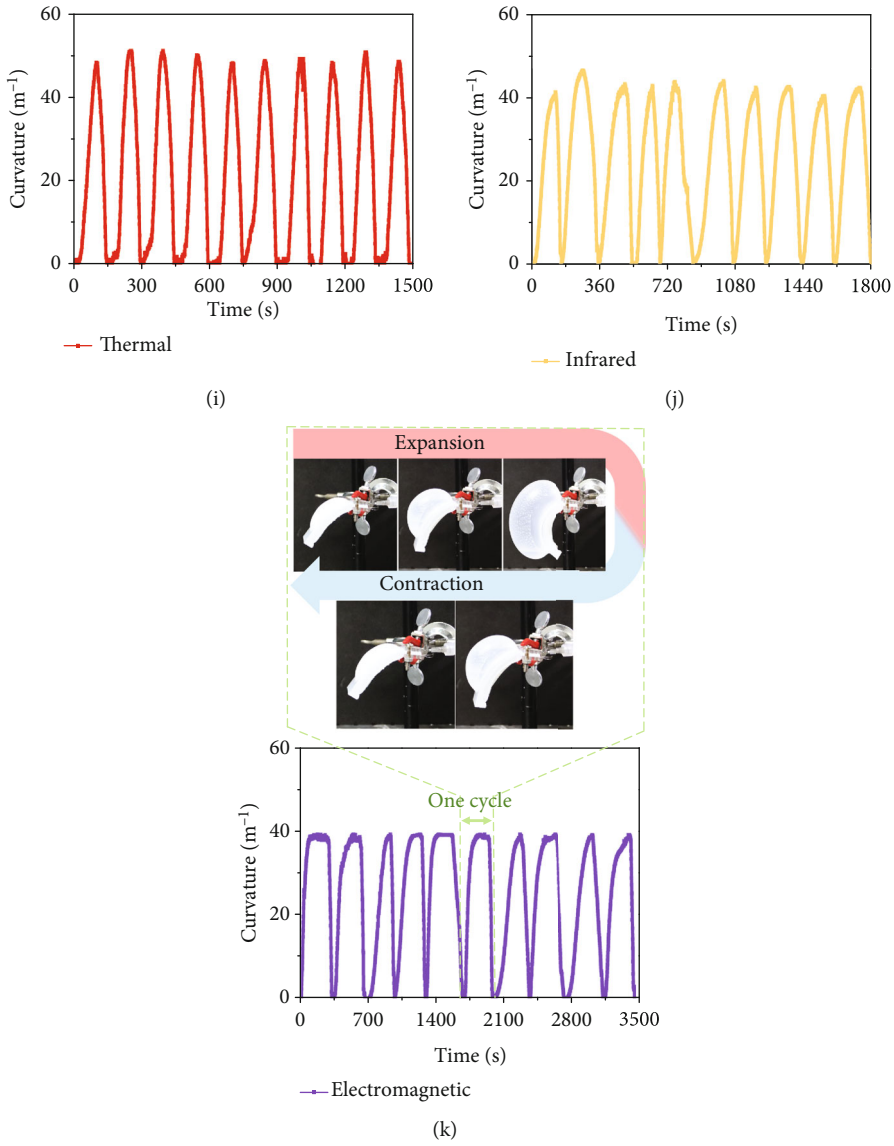

Figure 4: Changes in the (a) curvature and (b) force of the UTPSA as a function of distance under thermal blowing. Changes in the (c) curvature and (d) force of the UTPSA as a function of distance under infrared light. Changes in the (e) curvature and (f) force of the UTPSA as a function of distance under an electromagnetic field. Changes in the curvature of the UTPSA depending on the obstacle: (g) glass and (h) an alumina substrate. The cyclic performance of the UTPSA triggered by unobstructed (i) thermal blowing, (j) infrared light, and (k) electromagnetic field.

of 0, 0.6, 1.2, and 1.8 cm, respectively. Although the change in the distance was much smaller compared to other cases, the decrease in force with respect to distance was the highest among the three types of stimuli.

Figures 4(g) and 4(h) illustrate the UTPSA performance depending on the obstacle type. Changes in the curvature of the UTPSA were analyzed when glass or alumina substrates were placed in the middle of the delivery path of each stimulus source (Figure 1(d) and Figure S3). Figure 4(g) shows the case where a glass substrate is used as an obstacle. Thermal energy was unable to penetrate the glass substrate, making the operation of the UTPSA using thermal blowing impossible. By contrast, the UTPSA operation using infrared light was possible with the glass obstacle, exhibiting a maximum curvature of 39 m^{-1}. In comparison to the case with no obstacle, the curvature decreased by approximately 15%, whereas the time required for one cycle increased by 85% (from 124 to 229 s). For the electromagnetic field case, the maximum value of the curvature was 40 m^{-1}, which was reduced by 11% compared to the case without an obstacle, whereas the time required for one cycle increased to 287 s (12% increment).

Figure 4(h) illustrates the UTPSA operation when an alumina substrate is used as an obstacle. For the thermal blowing and infrared light cases, the UTPSA did not operate properly because the stimuli could not penetrate the ceramic obstacle (cf. Figures 3(b) and 3(d)). By contrast, for the electromagnetic field case, the UTPSA could operate despite the alumina substrate obstacle. Compared with the case without an obstacle, the UTPSA performance was degraded by 13%

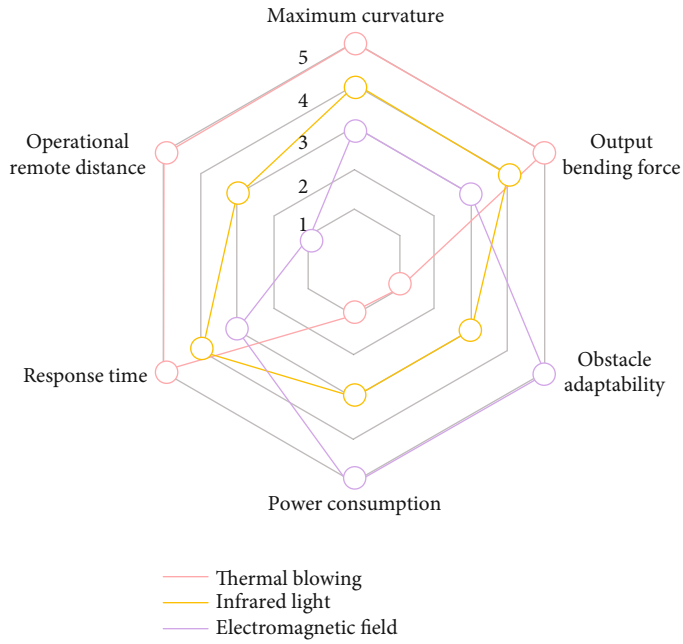

Figure 5: Comparative analysis using an arbitrary scale of 0 (poor performance) to 6 (good performance).

with a maximum curvature of 39 m^{-1}, whereas the operating time required for one cycle increased to 316 s (4% increment). As the dielectric obstacle is not a significant obstruction in the path of the propagation of the electromagnetic field, the UTPSA can operate normally. However, the electromagnetic field can be significantly hindered by the electromagnetic interference effects of ferromagnetic or conductive materials [43]. Figures 4(i)–4(k) illustrate the UTPSA performance over 10 cycles without an obstacle. For the thermal blowing, infrared light, and electromagnetic field cases, the distances between the stimulus source and UTPSA were 40, 10, and 0.6 cm, respectively. During the 10 cycles of bending motion, the performance was stable.

A comprehensive evaluation of the bending performance of the UTPSA is illustrated in Figure 5 with regard to (i) maximum curvature, (ii) operational remote distance, (iii) response time, (iv) obstacle adaptability, (v) output bending force, and (vi) power consumption. This comparison was performed using commercial equipment for each mechanism of the same UTPSA. The maximum curvature corresponding to the maximum bending of the UTPSA (cf. Figures 4(a), 4(c), and 4(e)) decreased in the order of thermal blowing (49.4 m^{-1}), infrared light (49.0 m^{-1}), and electromagnetic field (45.8 m^{-1}). The operational wireless distance, which indicates the maximum distance at which the UTPSA can operate, decreased in the order of thermal blowing (80 cm), infrared light (20 cm), and electromagnetic field (1.8 cm). The response rate (the bending rate), which was evaluated by dividing the maximum curvature with the time required for one cycle, exhibited a descending order, i.e., thermal blowing (0.56 $m^{-1}{\cdot}s^{-1}$), infrared light irradiation (0.4 $m^{-1}{\cdot}s^{-1}$), and electromagnetic field (0.15 $m^{-1}{\cdot}s^{-1}$) (cf. Figures 4(a), 4(c), and 4(e)). The electromagnetic field was the best among the three stimuli tested in terms of obstacle adaptability. With respect to the output force resulting from bending, the corresponding values decreased in the order of thermal blowing (900 mN), infrared light irradiation (800 mN), and electromagnetic field (610 mN) (cf. Figures 4(b), 4(d), and 4(f)). The power consumption of the operating UTPSA decreased in the order of thermal blowing (1600 W), infrared light irradiation (275 W), and electromagnetic field (12 W). The results indicated that there is no single best performer and the operating environment must be considered to select an appropriate stimulus to operate the UTPSA.

2.4. Application of UTPSA. To demonstrate its potential use, a UTPSA-based crawler was fabricated and evaluated (Figure 6). The fabrication process is detailed in Section S1.5 in the Supplementary Information file. Figures 6(a) and 6(b) depict the movement of the crawler, which comprises two stages: (i) straightened state and (ii) crouched state. Figure 6(a) illustrates the straightened state of the crawler on the ground when no external force is applied. Following the application of a wireless stimulus, the UTPSA crawler started to bend and transitioned to the crouched state. The left-hand side image in the middle row of Figure 6 illustrates the application of force during the inflation stage. During its bending motion (Figures 6(a) and 6(b)), a compressive force occurred and pulled the front and rear edges of the crawler to the center. Simultaneously, blades obliquely attached to the part under the crawler exerted different frictional forces according to the direction of motion. This orientation-dependent friction was attributed to the interlock in a specific direction between the oblique blades and uneven substrate (ground), which is a type of ratchet effect [44]. The crawler did not operate without the orientation-dependent friction (cf. without blades, Movie

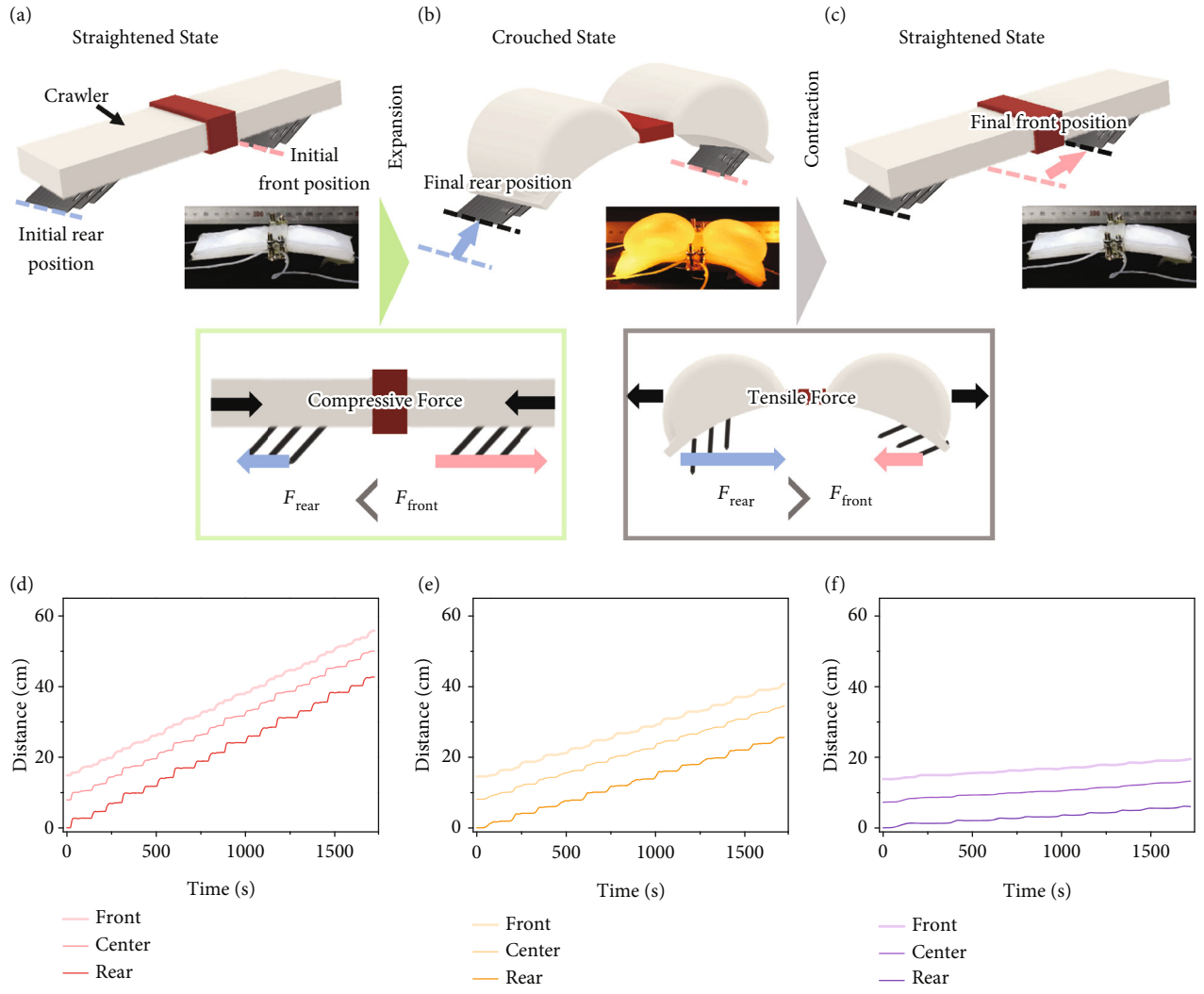

Figure 6: Movements of the UTPSA-based crawler: (a) initial straightened state, (b) crouched state, and (c) straightened state after moving forward. The travel distance of the crawler under different wireless stimuli: (d) thermal blowing, (e) infrared light, and (f) electromagnetic field.

S2). The force required to move the crawler forward was 0.15 N, whereas a force of 0.7 N was required for the backward direction. This crawling movement did not occur when the crawler was slightly inflated because the crawler's compressive force could not overcome the rear frictional force (0.7 N). Moreover, the overinflated UTPSA could not improve its movement, thus generating a compressive force, which exceeded the frontal frictional force (0.15 N). It made the crawler pull the legs to the center (Movie S2).

The crawler in the crouched state returned to its initial state through deflation. The right-hand side illustration in the middle row of Figure 6 shows the forces acting on the crawler during deflation. Through the deflation process, a tensile force from the center to the edges of the crawler was generated, causing the crawler to straighten. At this time, the rear blades facing down exerted a higher frictional force than the front blades facing up. Consequently, the front side of the crawler moved forward, and its rear side remained at rest (Figure 6(c)). By repeating this cycle, the crawler can keep moving forward, akin to the movement of a caterpillar [45].

Figures 6(d)–6(f) show the travel distances of the front, center, and rear parts of the crawler depending on different stimuli (cf. Figure S6 and Movie S3). Figure 6(d) shows the results obtained using thermal blowing. The time required and travel distance for a single cycle comprising bending and stretching were 123 s and 2.7 cm, respectively. The crawling speed and moving efficiency were 0.02 $cm \cdot s^{-1}$ and 0.06 $cm \cdot W^{-1} \cdot h^{-1}$, respectively. Note that the moving efficiency defined here as the distance covered by the crawler divided by the corresponding energy supply to the source. Figures 6(e) and 6(f) present the results corresponding to infrared light and electromagnetic field stimuli, respectively. The corresponding required times, travel distances, crawling speeds, and moving efficiencies for a single cycle of the infrared light and electromagnetic field were 170 and 290 s, 2 and 1.4 cm, 0.01 and 0.005 $cm \cdot s^{-1}$, and 0.181 and 0.75 $cm \cdot W^{-1} \cdot h^{-1}$, respectively. The travel performance of the crawler, depending on the stimuli, was consistent with the results of the actuation performance depicted in Figure 5.

3. Conclusion

Untethered nanotextured thermopneumatic soft actuators (UTPSAs) capable of inflation owing to the partial evaporation of the fluid in their elastomeric cavity can bend if one wall is made stiffer than the other, which causes self-buckling of the entire system, resulting in a bent configuration. The most suitable working fluid to encase in the cavity of the elastomeric body appears to be Novec 7000 because it possesses a low boiling point and high vapor pressure. The partial evaporation of the working fluid can be triggered by one of the following three wireless stimuli: (i) thermal blowing, (ii) irradiation with infrared light, and (iii) transmission of electromagnetic energy (which induces a current to cause the Joule heating of a wire embedded in the elastomeric body). The efficiencies of the first two stimuli were comprehensively examined as a function of the distance between the stimulus source and UTPSA, and that of the third stimulus was examined as a function of the distance between the coils. In the case of thermal blowing, the UTPSA operation can be quantified as follows: the bending-stretching cycles were completed in 88, 145, 305, and 455 s when the distances between the heat gun and UTPSA were 20, 40, 60, and 80 cm, respectively. In the case of infrared light irradiation, they were completed in 124, 179, 266, and 336 s when the distances between the lamp and UTPSA were 5, 10, 15, and 20 cm, respectively. In the case of electromagnetic field induction, the time periods were 313, 328, 351, and 371 s when the distances between the generating and receiving coils were 0, 0.6, 1.2, and 1.8 cm, respectively. In the presence (or absence) of an obstacle (a transparent glass shield or opaque alumina shield), the stimuli efficiency varied. The results revealed the less affected stimulus considering the presence of an obstacle and can help select the most appropriate stimulus for a specific operating environment. Moreover, a UTPSA in the form of a crawler, whose motion is similar to that of a caterpillar, was manufactured. Its multicycle crawling motion was related to a ratchet-like effect generated by the blades (installed in the front and back) in contact with the ground. As a result, a UTPSA can select an optimal operating mechanism for a specific environment and thus be useful under dynamic environmental conditions. However, for industrial applications, features such as movement speed, exerted force, and stable control distance need to be further analyzed and improved.

Data Availability

The data that support the findings of this study are available from the corresponding authors upon reasonable request.

Conflicts of Interest

The authors declare that they have no conflicts of interest.

Authors' Contributions

Yong Il Kim and Si Wung Kim contributed equally to this work.

Acknowledgments

This work was supported by the National Research Foundation of Korea (NRF) grant funded by the Korea government (NRF-2020R1A5A1018153, NRF-2021R1A2C2010530, and 2022M3J1A106422611).

Supplementary Materials

Details of the experimental procedure/setup, the method for calculating the curvature, results of light transmission through the obstacles, and motion of the UTPSA/crawler are provided in the supplementary materials. Figure S1: (a) UTPSA fabrication process and (b) the operating system. Figure S2: (a) measurement of the curvature of the UTPSA based on the three-point displacement. (b) Geometric equivalent. Figure S3: experimental setup to evaluate the remote control of the UTPSA when an obstacle is present between the stimulus source and UTPSA. Figure S4: infrared images of a light lamp with (a) glass and (b) alumina obstacles. The distance between the lamp and each obstacle was 10 cm. Figure S5: transmittance profiles of the glass and alumina obstacles within the visible and infrared wavelength range. Figure S6: experimental setups for the crawler: (a) thermal blowing, (b) infrared light irradiation, and (c) transmission of electromagnetic flux. Dual sources were used to stimulate each half of the crawler (the crawler was constructed using two UTPSAs). Movie S1: motion of UTPSA without a passive layer. Movie S2: motion of the crawler without blades. Movie S3: motion of the crawler depending on different stimuli. *(Supplementary Materials)*

References

[1] C. Majidi, "Soft robotics: a perspective—current trends and prospects for the future," *Soft Robotics*, vol. 1, no. 1, pp. 5–11, 2014.

[2] R. F. Shepherd, F. Ilievski, W. Choi et al., *Multigait Soft Robot*, PNAS, 2011.

[3] J. R. Allison, C. C. Currie, D. C. Edwards et al., "Evaluating aerosol and splatter following dental procedures: addressing new challenges for oral health care and rehabilitation," *Journal of Oral Rehabilitation*, vol. 48, no. 1, pp. 61–72, 2021.

[4] D. Copaci, J. Munoz, I. González, C. A. Monje, and L. Moreno, "SMA-driven soft robotic neck: design, control and validation," *IEEE Access*, vol. 8, pp. 199492–199502, 2020.

[5] Z. Samadikhoshkho, K. Zareinia, and F. Janabi-Sharifi, "A Brief Review on Robotic Grippers Classifications," in *2019 IEEE Canadian Conference of Electrical and Computer Engineering (CCECE)*, Edmonton, AB, Canada, 2019.

[6] K. Nakajima, H. Hauser, T. Li, and R. Pfeifer, "Exploiting the dynamics of soft materials for machine learning," *Soft Robotics*, vol. 5, no. 3, pp. 339–347, 2018.

[7] S. An, D. J. Kang, and A. L. Yarin, "A blister-like soft nanotextured thermo-pneumatic actuator as an artificial muscle," *Nanoscale*, vol. 10, no. 35, pp. 16591–16600, 2018.

[8] R. Pelrine, R. Kornbluh, and G. Kofod, "High-strain actuator materials based on dielectric elastomers," *Advanced Materials*, vol. 12, no. 16, pp. 1223–1225, 2000.

[9] C. Huang, T. Tan, Z. Wang et al., "Origami dynamics based soft piezoelectric energy harvester for machine learning

assisted self-powered gait biometric identification," *Energy Conversion and Management*, vol. 263, article 115720, 2022.

[10] Y. Yu and T. Ikeda, "Soft actuators based on liquid-crystalline elastomers," *Angewandte Chemie International Edition*, vol. 45, no. 33, pp. 5416–5418, 2006.

[11] G. Filipcsei, J. Feher, and M. Zrınyi, "Electric field sensitive neutral polymer gels," *Journal of Molecular Structure*, vol. 554, no. 1, pp. 109–117, 2000.

[12] S.-K. Ahn, R. M. Kasi, S.-C. Kim, N. Sharma, and Y. Zhou, "Stimuli-responsive polymer gels," *Soft Matter*, vol. 4, no. 6, pp. 1151–1157, 2008.

[13] D. Kuckling, A. Richter, and K. F. Arndt, "Temperature and pH-dependent swelling behavior of poly(N-isopropylacrylamide) copolymer hydrogels and their use in flow control," *Macromolecular Materials and Engineering*, vol. 288, no. 2, pp. 144–151, 2003.

[14] H. Shigemune, S. Maeda, Y. Hara, N. Hosoya, and S. Hashimoto, "Origami robot: a self-folding paper robot with an electrothermal actuator created by printing," *IEEE/ASME Transactions on Mechatronics*, vol. 21, no. 6, pp. 2746–2754, 2016.

[15] M.-A. Lacasse, V. Duchaine, and C. Gosselin, "Characterization of the Electrical Resistance of Carbon-Black-Filled Silicone: Application to a Flexible and Stretchable Robot Skin," in *2010 IEEE International Conference on Robotics and Automation*, Anchorage, AK, USA, 2010.

[16] M. Ma, L. Guo, D. G. Anderson, and R. Langer, "Bio-inspired polymer composite actuator and generator driven by water gradients," *Science*, vol. 339, no. 6116, pp. 186–189, 2013.

[17] L. Hines, K. Petersen, G. Z. Lum, and M. Sitti, "Soft actuators for small-scale robotics," *Advanced Materials*, vol. 29, no. 13, article 1603483, 2017.

[18] J. Shintake, H. Sonar, E. Piskarev, J. Paik, and D. Floreano, "Soft pneumatic gelatin actuator for edible robotics," in *IEEE/RSJ International Conference on Intelligent Robots and Systems*, pp. 6221–6226, Vancouver, BC, Canada, 2017.

[19] J. So, U. Kim, Y. B. Kim et al., "Shape estimation of soft manipulator using stretchable sensor," *Cyborg and Bionic Systems*, vol. 2021, pp. 1–10, 2021.

[20] D. Liu, X. Liu, Z. Chen et al., "Magnetically driven soft continuum microrobot for intravascular operations in microscale," *Cyborg and Bionic Systems*, vol. 2022, article 9850832, 8 pages, 2022.

[21] C. Huang, Z. Lai, X. Wu, and T. Xu, "Multimodal locomotion and cargo transportation of magnetically actuated quadruped soft microrobots," *Cyborg and Bionic Systems*, vol. 2022, 2022.

[22] K. Suzumori, S. Endo, T. Kanda, N. Kato, and H. Suzuki, "A bending pneumatic rubber actuator realizing soft-bodied manta swimming robot," in *IEEE International Conference on Robotics and Automation*, pp. 4975–4980, Rome, Italy, 2007.

[23] R. V. Martinez, A. C. Glavan, C. Keplinger, A. I. Oyetibo, and G. M. Whitesides, "Soft actuators and robots that are resistant to mechanical damage," *Advanced Functional Materials*, vol. 24, no. 20, pp. 3003–3010, 2014.

[24] L. Liu, A. Ghaemi, S. Gekle, and S. Agarwal, "One-component dual actuation: poly(NIPAM) can actuate to stable 3D forms with reversible size change," *Advanced Materials*, vol. 28, no. 44, pp. 9792–9796, 2016.

[25] D. J. Kang, S. An, A. L. Yarin, and S. Anand, "Programmable soft robotics based on nano-textured thermo-responsive actuators," *Nanoscale*, vol. 11, no. 4, pp. 2065–2070, 2019.

[26] Y. I. Kim, S. An, A. L. Yarin, and S. S. Yoon, "Performance enhancement of soft nanotextured thermopneumatic actuator by incorporating silver nanowires into elastomer body," *Soft Robotics*, vol. 8, no. 6, pp. 711–719, 2021.

[27] Y. I. Kim, S. An, C. Park et al., "Nanotextured soft electrothermo-pneumatic actuator for constructing lightweight, integrated, and untethered soft robotics," *Soft Robotics*, vol. 9, no. 5, pp. 960–969, 2022.

[28] Y. Tang and J. Yin, "Design of multifunctional soft doming actuator for soft machines," *Advanced Materials Technologies*, vol. 3, no. 7, article 1800069, 2018.

[29] S. Wang, H. Luo, C. Linghu, and J. Song, "Elastic energy storage enabled magnetically actuated, octopus-inspired smart adhesive," *Advanced Functional Materials*, vol. 31, no. 9, article 2009217, 2021.

[30] Y. W. Lee, S. Chun, D. Son, X. Hu, M. Schneider, and M. Sitti, "A tissue adhesion-controllable and biocompatible small-scale hydrogel adhesive robot," *Advanced Materials*, vol. 34, no. 13, article 2109325, 2022.

[31] R. Hilzinger and W. Rodewald, *Magnetic Materials: Fundamentals, Products, Properties, Applications*, Vacuumschmelze GmbH & Co, Hanau, Germany, 2013.

[32] A. Miriyev, K. Stack, and H. Lipson, "Soft material for soft actuators," *Nature Communications*, vol. 8, no. 1, p. 596, 2017.

[33] G. Decroly, R. Raffoul, C. Deslypere et al., "Optimization of phase-change material–elastomer composite and integration in kirigami-inspired voxel-based actuators," *Frontiers in Robotics and AI*, vol. 8, article 672934, 2021.

[34] S. Senzaki, T. Akagi, S. Dohta, and Y. Fujiwara, "Development and analysis of flexible thin actuator with a built-in fluid pressure source," *EDP Sciences*, vol. 51, article 02005, 2016.

[35] Y. Nishikawa and M. Matsumoto, "A design of fully soft robot actuated by gas–liquid phase change," *Advanced Robotics*, vol. 33, no. 12, pp. 567–575, 2019.

[36] R. Uramune, H. Ishizuka, T. Hiraki, Y. Kawahara, S. Ikeda, and O. Oshiro, "HaPouch: a miniaturized, soft, and wearable haptic display device using a liquid-to-gas phase change actuator," *IEEE Access*, vol. 10, pp. 16830–16842, 2022.

[37] J. J. Licari and D. W. Swanson, "Chapter 7 - test and inspection methods," in *Adhesives Technology for Electronic Applications*, J. J. Licari and D. W. Swanson, Eds., pp. 345–377, William Andrew Publishing, Oxford, English, Second Edition edition, 2011.

[38] B. P. Jelle, A. Gustavsen, T. N. Nilsen, and T. Jacobsen, "Solar material protection factor (SMPF) and solar skin protection factor (SSPF) for window panes and other glass structures in buildings," *Solar Energy Materials and Solar Cells*, vol. 91, no. 4, pp. 342–354, 2007.

[39] B. Adelmann and R. Hellmann, "Numerical and experimental study on flexural strength of laser microstructured alumina," *Advances in Ceramic Science and Engineering*, vol. 5, pp. 28–34, 2016.

[40] Y. H. Lho, "A study on transmission efficiency of wireless power induction and resonant charging methodologies," *Journal of IKEEE*, vol. 23, no. 2, pp. 747–750, 2019.

[41] J. Chen, X. Liu, Z. Chi, X. Li, D. Jiao, and S. Zeng, "Research on efficiency of contactless charging system based on electromagnetic induction," *EDP Sciences*, vol. 40, p. 07005, 2016.

[42] W. Ke, L. Chengxi, and S. Huizhong, "Optimal Design of Electromagnetic Induction High-Efficiency Wireless Power Transmission System," in *2020 International Conference on*

Electrical Engineering and Control Technologies (CEECT), Melbourne, VIC, Australia, 2020.

[43] D. Chung, "Materials for electromagnetic interference shielding," *Materials Chemistry and Physics*, vol. 255, article 123587, 2020.

[44] H. T. Tramsen, S. N. Gorb, H. Zhang, P. Manoonpong, Z. Dai, and L. Heepe, "Inversion of friction anisotropy in a bio-inspired asymmetrically structured surface," *Journal of the Royal Society Interface*, vol. 15, no. 138, p. 20170629, 2018.

[45] X. Wang, B. Yang, D. Tan et al., "Bioinspired footed soft robot with unidirectional all-terrain mobility," *Materials Today*, vol. 35, pp. 42–49, 2020.